



Cite this: *Energy Adv.*, 2022, 1, 146

## Enhancing the photocatalytic hydrogen generation performance and strain regulation of the vertical $\text{Gel}_2/\text{C}_2\text{N}$ van der Waals heterostructure: insights from first-principles study†

Francis Opoku, \*<sup>a</sup> Samuel Osei-Bonsu Oppong, <sup>b</sup> Noah Kyame Asare-Donkor, <sup>a</sup> Osei Akoto<sup>a</sup> and Anthony Apeke Adimado<sup>a</sup>

A suitable electronic structure and efficient charge separation are significant for the performance of photocatalytic water splitting. Herein, we have designed a two-dimensional  $\text{Gel}_2/\text{C}_2\text{N}$  van der Waals (vdW) heterostructure and systematically examined its stability, electronic, photocatalytic, optoelectronic and optical properties, and the effects of applying biaxial strain using density functional theory calculations. Based on *ab initio* molecular dynamic simulations and phonon dispersion calculations, the dynamic and thermal stability of the  $\text{Gel}_2/\text{C}_2\text{N}$  vdW heterostructure was confirmed. The  $\text{Gel}_2/\text{C}_2\text{N}$  vdW heterostructure showed an inherent type-II indirect bandgap energy of 2.02 eV and excellent visible light absorption, which were significantly improved compared to those of the monolayers. The projected band structure showed that the valence band minimum and conduction band maximum were contributed by the  $\text{C}_2\text{N}$  and  $\text{Gel}_2$  monolayers, respectively, which was favourable for efficient charge separation, thus increasing the solar energy conversion. Moreover, the  $\text{Gel}_2/\text{C}_2\text{N}$  vdW heterostructure band edges precisely straddled the water redox potential energies for pH values ranging from 0 to 9, allowing it to meet the conditions for spontaneous water splitting. The charge density difference revealed that about 0.263 electrons were transferred from the  $\text{C}_2\text{N}$  to  $\text{Gel}_2$  monolayer, and the potential drop at the interface was estimated to be 7.16 eV. We further hypothesised that strain might be utilised to tune the band edges and bandgap of the  $\text{Gel}_2/\text{C}_2\text{N}$  vdW heterostructure, resulting in a transition from a type-II indirect to a type-I direct bandgap semiconductor under tensile biaxial strain. Our findings provide a theoretical design for strategies to improve the performance of  $\text{Gel}_2/\text{C}_2\text{N}$  in solar conversion, nanoelectronic and optoelectronic devices.

Received 1st November 2021,  
Accepted 19th January 2022

DOI: 10.1039/d1ya00047k

rsc.li/energy-advances

### I. Introduction

Given the scarcity of fossil fuels and the deterioration of the environment, developing clean and sustainable alternative energy sources that are renewable, cost-effective, environmentally friendly and can be replenished is urgently required to address the energy demands and ever-growing pollution of the environment.<sup>1,2</sup> The strong demand for renewable energy has created a research hotspot to explore high-efficiency photocatalyst and photovoltaic materials. Today, to address the energy

scarcity and environmental pollution, hydrogen ( $\text{H}_2$ ) produced by photocatalytic water splitting<sup>3–5</sup> has emerged as a viable alternative to fossil fuels due to its zero pollutant emission (the only combustion product is water vapour), higher energy density per unit mass, and lightweight, the abundance of solar energy and the fact that it is the highest energy carrier.<sup>6</sup> <https://0-pubs-rsc-org.ujlink.uj.ac.za/en/content/articlehtml/2021/ta/d1ta04256d?page=search-cit3>. After overall water splitting was experimentally achieved with  $\text{TiO}_2$ ,<sup>7</sup> several photocatalysts, such as metal nitrides, sulphides and oxides, and other bulk materials, have been reported to play a vital role in solar energy conversion and storage processes.<sup>8</sup> However, the low solar utilisation of bulk materials hinders their practical applications as high-efficiency photocatalysts.

After successful fabrication of graphene, other two-dimensional (2D) materials, such as black phosphorene, monochalcogenides,

<sup>a</sup> Department of Chemistry, Kwame Nkrumah University of Science and Technology, Kumasi, Ghana. E-mail: ofrancis2010@gmail.com

<sup>b</sup> Marine Engineering Department, Regional Maritime University, P.O. Box GP 1115, Accra, Ghana

† Electronic supplementary information (ESI) available. See DOI: 10.1039/d1ya00047k



silicene, graphite-like carbon nitride, MXenes, stanene, transition metal dichalcogenides and others,<sup>9–12</sup> exfoliated from their bulk materials, have been fabricated experimentally and predicted theoretically,<sup>13</sup> showing great potential for photocatalytic water splitting.<sup>14</sup> For practical applications, a promising 2D photocatalyst semiconductor must possess a small exciton binding energy, low exciton recombination rate and high separation efficiency of photo-generated charge carriers, a bandgap value greater than 1.23 eV, sufficiently large specific surface area, good visible light response and appropriate band edge positions for overall water splitting.<sup>15</sup>

Carbon nitride ( $C_2N$ ), a novel 2D layered semiconductor material, was successfully synthesised by thermally depositing a  $C_2N$ -h2D crystal sample on a Cu(111) substrate *via* a simple bottom-up wet-chemical reaction technique.<sup>16</sup> Based on their bonding analyses, the C–N bonds in  $C_2N$  exhibit  $sp^2$  hybridisation comparable to the C–C bonds in graphene.<sup>17</sup> The primary distinction between 2D  $C_2N$  and graphene is that the  $C_2N$  layer has periodic holes in the form of a delocalised benzene structure. The two aromatic rings are joined together by pyrazine rings that are made up of a six-membered  $D_{2h}$  point group with two N atoms facing one another. Recently, carbon nitride materials, including  $C_2N$ ,  $C_6N_6$  and  $C_3N_4$ ,<sup>18,19</sup> have been identified as potential photocatalysts due to their good biocompatibility, non-toxicity, abundance and low cost.  $C_2N$  has high water permeability, superior chemical activity and better visible light absorption than the other carbon nitride materials.<sup>20</sup>  $C_2N$  has an excellent direct bandgap and optical properties, and has been demonstrated experimentally as an effective  $H_2$  generation photocatalyst.<sup>21</sup> Because N and C are lighter elements, the hydrogen storage capacity of  $C_2N$  may be significant as a result of its high surface-to-volume ratio compared to other 2D materials.<sup>6</sup> 2D germanium iodide ( $GeI_2$ ) has potential in solar cells, and electronic and optoelectronic devices.<sup>22</sup> Ozisik *et al.*<sup>23</sup> found that  $GeI_2$  is thermodynamically and mechanically stable. Though 2D materials may provide more efficient redox reactions than their bulk equivalents, their photocatalytic efficacy is limited due to the high electron–hole recombination rate because the orbitals in the conduction band (CB) and valence band (VB) are not completely separated in space.<sup>24</sup>  $C_2N$  also suffers from a significantly high electron–hole recombination rate, which prohibits its further applications.<sup>25,26</sup> As a result, a technique for the effective separation of photogenerated charge carriers must be investigated as soon as possible.

Recently, van der Waals (vdW) heterostructures have been developed to boost the optical, electronic and photocatalytic properties of 2D materials.<sup>27,28</sup> Experimentally, vdW heterostructures can be obtained by direct growth and mechanical assembly,<sup>29</sup> while theoretically they can be predicted by stacking two or more 2D materials on top of each other.<sup>30</sup> 2D heterostructures are energetically stable and undergo easy exfoliation since the two materials are held together by weak vdW interactions. Recently, type-II heterostructures have attracted much attention since they can effectively separate photogenerated charge carriers to different sheets for  $H_2$  and  $O_2$  generation.<sup>31,32</sup> Several type-II  $C_2N$ -based heterostructures, such as  $C_2N$ /BlueP,<sup>33</sup> GeC/ $C_2N$ ,<sup>26</sup> BCN/ $C_2N$ ,<sup>34</sup>  $C_2N$ /MoSe<sub>2</sub>,<sup>35</sup>

$C_2N$ /InTe,<sup>36</sup>  $C_2N$ /GaTe,<sup>37</sup> g- $C_3N_4$ / $C_2N$ ,<sup>38</sup>  $C_2N$ /WS<sub>2</sub>,<sup>39</sup>  $C_2N$ /MoS<sub>2</sub>,<sup>40</sup> GaX/ $C_2N$  (X = S, Se)<sup>41,42</sup> and  $C_2N$ /GaTe,<sup>36</sup> have exhibited high power conversion efficiency with enhanced photocatalytic/photovoltaic performance compared to isolated  $C_2N$  due to the improved separation of electrons. <https://doi.org/10.1039/C9CP06696A> page = search - cit31.

The search for suitable 2D materials to create type-II heterostructures opens up a wide range of possibilities for photocatalytic water splitting to generate  $H_2$ . Surprisingly, the lattice constant of the  $GeI_2$  monolayer is almost double that of  $C_2N$ . Given this, the new  $GeI_2$ / $C_2N$  vdW heterostructure might be an effective material with better photocatalytic activity than  $C_2N$ . Therefore, the small lattice mismatch between the  $GeI_2$  monolayer and  $C_2N$  makes the experimental fabrication of a vdW heterostructure highly achievable. The reason for using  $C_2N$  is that it has the properties of a direct bandgap and high  $H_2$  storage capability. The successful exfoliation of 2D  $GeI_2$  and  $C_2N$  also provides more possibilities for designing  $GeI_2$ / $C_2N$  heterostructures. The newly designed 2D vdW heterostructure can enhance the electronic and optical properties of the isolated monolayers and overcome the limitation of their applicability in many fields. Using density functional theory (DFT) calculations, this study explores the photocatalytic performance, and structural, optical and electronic properties of 2D vertical  $GeI_2$ / $C_2N$  heterostructures (DFT). It is not easy to provide an adequate theoretical explanation of the electrical characteristics of the ground and excited states of 2D materials. Excitation or optical absorption is a more difficult task. The theoretical techniques available include the Bethe–Salpeter equation (BSE)<sup>43</sup> and time-dependent DFT (TD-DFT)<sup>44,45</sup> The former includes excitonic phenomena that are important for 2D materials. However, local relaxation and electron–phonon coupling effects are difficult to include. After being tested in many systems, the BSE approach<sup>46</sup> has been shown to be a dependable tool, but it also has drawbacks: long processing durations, especially for complex systems, and not necessarily well-adjusted approximations for the vertex function in solving the BS equation.<sup>44</sup> TDDFT, on the other hand, is free of the aforementioned shortcomings, as it is computationally significantly less costly and does not require any approximation for the exchange–correlation (XC) potential. TDDFT, an effective theory of charge density in which the effects of electron–electron interactions and hence all nontrivial excitations are characterized by the XC potential, is the dominant current *ab initio* technique for studying excitations in finite systems and solids.<sup>45</sup> In this study, we employ a simplified but effective TDDFT approach to simulate the optical properties of semiconducting materials. Through *ab initio* molecular dynamics (AIMD) and phonon dispersion calculations, the thermal and dynamic stabilities of the optimised structures were analysed. The band edges and the bandgap width, which are a research focus in photocatalysis, can be effectively modulated by strain.<sup>47–49</sup> Moreover, the electronic properties of isolated 2D  $GeI_2$  monolayers and  $C_2N$  can be easily modulated by applying strain.<sup>21,50</sup> With this in mind, we examine how strain may be



used to adjust the bandgap and band alignment of the  $\text{GeI}_2/\text{C}_2\text{N}$  heterostructure. Our theoretical findings suggest that the  $\text{GeI}_2/\text{C}_2\text{N}$  heterostructure can be utilised to develop novel electronics, optoelectronics and photocatalyst devices.

## II. Computational details

First-principles calculations were performed using the Quantum ESPRESSO package.<sup>51</sup> For structural relaxations, the generalised gradient approximation of Perdew–Burke–Ernzerhof was employed to account for the XC effects.<sup>52</sup> The conjugate-gradient technique<sup>53</sup> of Broyden–Fletcher–Goldfarb–Shannon (BFGS) was used for all the structural optimisations with the variable-cell relaxation method. We employ optimised norm-conserving Vanderbilt pseudopotentials<sup>54</sup> to account for the electron–ion interaction. A large vacuum of 30 Å was added to prevent the interactions of the periodic images. This vacuum distance was wide enough not to affect the band positions with reference to the vacuum energy level. Besides, the vdW interaction between the two monolayers was treated using the Grimme D3 method with Becke–Johnson damping dispersion correction.<sup>55,56</sup> The Brillouin zone integration was sampled using a Monkhorst–Pack grid<sup>57</sup> of  $7 \times 7 \times 1$ . The plane wave cutoff energy, the energy convergence criteria and the Hellmann–Feynman force of 55 Ry,  $10^{-6}$  Ry and  $10^{-3}$  Ry Bohr<sup>-1</sup>, respectively, are sufficient to give well-converged results. The harmonic interatomic force constants and phonon dispersions were calculated with density functional perturbation theory.<sup>58</sup> Due to the underestimation of the bandgap by the generalised gradient approximation of the Perdew–Burke–Ernzerhof functional,<sup>59</sup> the Heyd–Scuseria–Ernzerhof functional (HSE06)<sup>60</sup> with the fraction of exact local exchange of

0.25 and screening parameter of 0.2 Å<sup>-1</sup> was used to obtain accurate optical and electronic properties, with band structures drawn using the Wannier90 package.<sup>61</sup> Optical properties were calculated using the time-dependent density functional theory (TDDFT) method<sup>62,63</sup> within the Quantum ESPRESSO code.<sup>51</sup> The *NVT* ensemble with a Nosé–Hoover thermostat<sup>64,65</sup> at room temperature (300 K) was used to examine the thermal stability of the  $\text{GeI}_2/\text{C}_2\text{N}$  heterostructures. We utilised the XCrySDen package<sup>66</sup> to visualise the optimised structures, charge density and electron localisation function.

## III. Results and discussion

Before exploring the vdW heterostructures, the structural and electronic properties of  $\text{C}_2\text{N}$  and  $\text{GeI}_2$  were initially studied, as shown in Fig. 1.

The optimised lattice constants are  $a = b = 4.213$  Å for the  $\text{GeI}_2$  monolayer and  $a = b = 8.332$  Å for  $\text{C}_2\text{N}$ , which agreed with earlier experimental and theoretical data.<sup>67,68</sup> The C–C bond lengths in the pyrazine and benzene rings are 1.428 and 1.465 Å, respectively, and the C–N bond length is 1.335 Å for the optimised  $\text{C}_2\text{N}$  (Fig. 1a), which agreed with results from earlier studies.<sup>67,69</sup> To understand the effect of interlayer interaction, the change in bandgap along the  $\Gamma$ –M–K– $\Gamma$  high-symmetry direction between the isolated monolayers and the heterostructure was systematically studied. The  $\text{C}_2\text{N}$  band structure in Fig. 1b is a direct bandgap semiconductor (2.25 eV), which agrees with an earlier study.<sup>70</sup> Because the experimental measurement is done on multilayer materials,<sup>70</sup> this value is higher than the experimental value (1.96 eV).<sup>71</sup> The valence band maximum (VBM) and conduction band minimum (CBM) of  $\text{C}_2\text{N}$  are at the  $\Gamma$  point. Our findings show that the

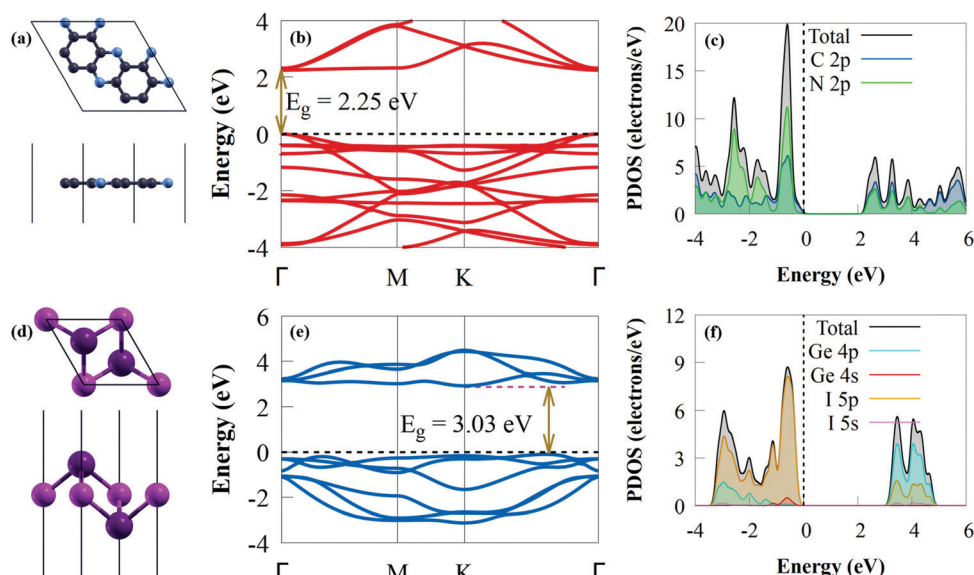


Fig. 1 The (a) optimised structure, (b) electronic band structure and (c) PDOS of  $\text{C}_2\text{N}$ . The (d) optimised structure, (e) electronic band structure and (f) PDOS of the  $\text{GeI}_2$  monolayer. Ge, I, C and N atoms are denoted as magenta, purple, grey and blue balls, respectively. The Fermi energy level is set as 0 by the black dashed line.



VBM and CBM mostly consist of C 2p and N 2p states, respectively (Fig. 1c), where the contribution of the C 2p orbital to the CB is quite dominant. The Ge–I bond length is about 3.005 Å in the case of the GeI<sub>2</sub> monolayer (Fig. 1d). The GeI<sub>2</sub> monolayer has indirect semiconductor properties (Fig. 1e) with a bandgap energy of 3.03 eV. This agrees with earlier results (3.05 eV).<sup>72</sup> The CBM and VBM are positioned on the *K* point and *K*– $\Gamma$  path, respectively. The calculated projected density of states (PDOS) (see Fig. 1f) shows that the VBM comprises 1 5p states, while the Ge 4p states mainly contribute to the CBM.

The GeI<sub>2</sub>/C<sub>2</sub>N vdW heterostructure in Fig. 2a is constructed by stacking a 4 × 4 supercell of GeI<sub>2</sub> monolayer on a 2 × 2 supercell of C<sub>2</sub>N. In general, a stable heterojunction may favourably form when the lattice mismatch is less than 5%.<sup>73,74</sup> For the GeI<sub>2</sub>/C<sub>2</sub>N vdW heterostructure, the lattice mismatch is only 1.06% along the *a* and *b* axes, which is relatively small compared to the acceptable maximum epitaxial growth value of 5%,<sup>75</sup> ensuring the experimental feasibility.<sup>37,76–78</sup> Moreover, the optimised interlayer distance between the GeI<sub>2</sub> monolayer and C<sub>2</sub>N is 3.374 Å.

The structural stability of the GeI<sub>2</sub>/C<sub>2</sub>N heterostructure is verified under different conditions. Firstly, to confirm the stability of the GeI<sub>2</sub>/C<sub>2</sub>N vdW heterostructure, the interfacial binding energy ( $\Delta E$ ) is examined:

$$\Delta E = (E_{\text{GeI}_2/\text{C}_2\text{N}} - E_{\text{GeI}_2} - E_{\text{C}_2\text{N}})/S \quad (1)$$

where  $E_{\text{GeI}_2/\text{C}_2\text{N}}$ ,  $E_{\text{GeI}_2}$  and  $E_{\text{C}_2\text{N}}$  are the total energies of the GeI<sub>2</sub>/C<sub>2</sub>N vdW heterostructure, C<sub>2</sub>N and GeI<sub>2</sub> monolayer, respectively, and  $S$  is the contact area. The results show that the calculated  $\Delta E$  of the GeI<sub>2</sub>/C<sub>2</sub>N heterostructure is  $-14.94 \text{ meV } \text{\AA}^{-2}$ , which is more negative than those of other C<sub>2</sub>N-based heterostructures, such as In<sub>2</sub>SeTe/C<sub>2</sub>N ( $-9.46$  to  $-11.84 \text{ meV } \text{\AA}^{-2}$ )<sup>79</sup> and C<sub>2</sub>N/GaTe (InTe) ( $-10.8$  ( $-9.6$ )  $\text{meV } \text{\AA}^{-2}$ ) heterostructures,<sup>76</sup> indicating that the GeI<sub>2</sub>/C<sub>2</sub>N vdW heterostructure should possess better stability. The computed  $\Delta E$  falls within the normal vdW interfacial binding energy range of  $-13$  to  $-21 \text{ meV } \text{\AA}^{-2}$ .<sup>80</sup> Moreover, the negative binding energy suggests that the fabrication of the GeI<sub>2</sub>/C<sub>2</sub>N vdW heterostructures is thermodynamically feasible.

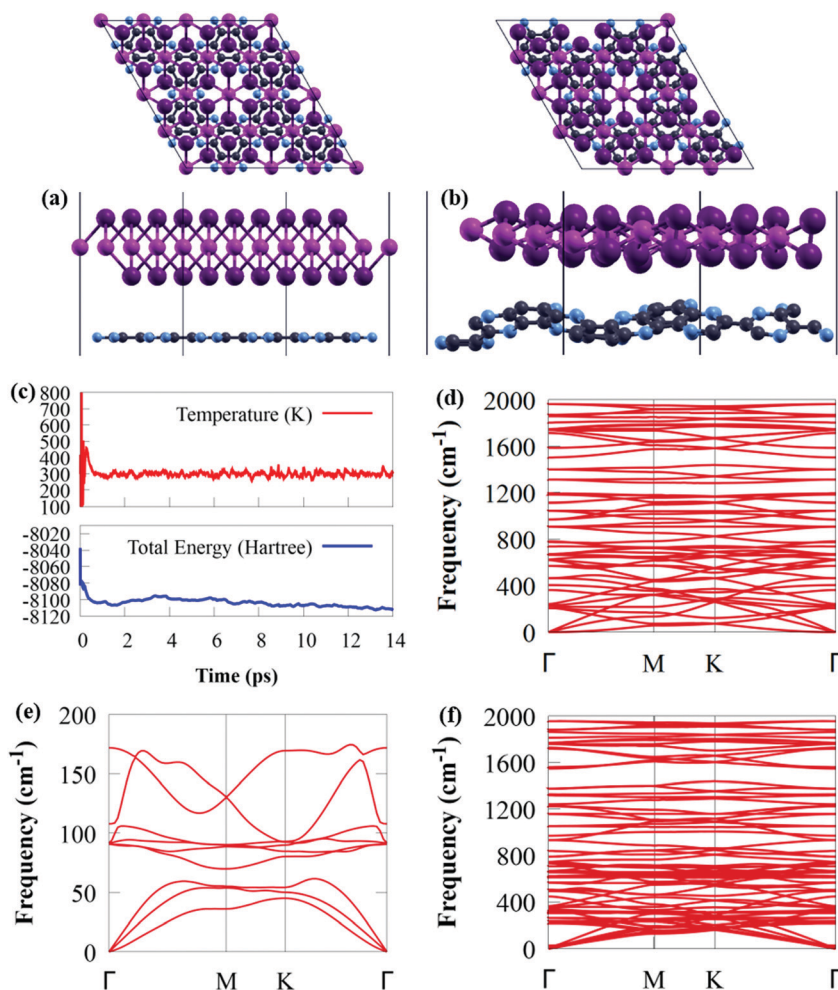


Fig. 2 (a) The top (top) and side (bottom) views of the optimised structure of the GeI<sub>2</sub>/C<sub>2</sub>N vdW heterostructure. (b) Top (top) and side (bottom) views of an AIMD simulations snapshot at room temperature. (c) Variation in total potential energy and temperature after 14 ps in the AIMD simulation at 300 K. Phonon dispersion spectra of (d) C<sub>2</sub>N, (e) the GeI<sub>2</sub> monolayer and (f) the GeI<sub>2</sub>/C<sub>2</sub>N vdW heterostructure. Grey, blue, magenta and purple balls denote C, N, Ge and I atoms, respectively.

Thermal stability is extremely important in photocatalysis. Before delving into the electronic properties of the  $\text{GeI}_2/\text{C}_2\text{N}$  vdW heterostructure, AIMD simulations and phonon dispersion calculations were used to ensure its thermodynamic stability. The AIMD simulation shows that the  $\text{GeI}_2/\text{C}_2\text{N}$  heterostructure retained its structure with no bonds broken at 300 K after heating for 14 ps, as shown in Fig. 2b. Furthermore, the difference in total energy and temperature in Fig. 2c before and after 14 ps is quite small. As a result, at room temperature, the  $\text{GeI}_2/\text{C}_2\text{N}$  vdW heterostructure is thermally stable. The phonon spectra of the  $\text{GeI}_2$  monolayer and  $\text{C}_2\text{N}$  were computed, as shown in Fig. 2d and e. The absence of negative frequency in the phonon spectra confirms that the  $\text{GeI}_2$  monolayer and  $\text{C}_2\text{N}$  are dynamically stable. It is worth mentioning that no imaginary phonon mode is observed in the  $\text{GeI}_2/\text{C}_2\text{N}$  vdW heterostructure across the Brillouin zone, indicating its dynamic stability.

Having verified the experimental feasibility and the intrinsic stability of the  $\text{GeI}_2/\text{C}_2\text{N}$  vdW heterostructure, we evaluated the projected band structure, as shown in Fig. 3a, to further analyse the change in electronic properties.

The electronic band structures of the  $\text{GeI}_2$  monolayer and  $\text{C}_2\text{N}$  are well retained after creating the  $\text{GeI}_2/\text{C}_2\text{N}$  heterostructure, indicating the weak interaction between the  $\text{GeI}_2$  monolayer and  $\text{C}_2\text{N}$ . The indirect bandgap of the  $\text{GeI}_2/\text{C}_2\text{N}$  vdW heterostructure is 2.02 eV, which is less than those of the  $\text{GeI}_2$  monolayer and  $\text{C}_2\text{N}$ . The bandgap was slightly lower than those of  $\text{CdSe}/\text{C}_2\text{N}$  (2.12 eV),<sup>78</sup> h-BN/ $\text{C}_2\text{N}$  (2.30 eV),<sup>26</sup> blueP/g-GeC (2.213 eV),<sup>81</sup> WSSe/BSe (2.151 eV),<sup>82</sup> and WSSe/g-GaN (2.39 eV)<sup>83</sup> vdW heterostructures, but slightly higher than that of the  $\text{C}_2\text{N}/\text{g-ZnO}$  heterostructure (2 eV).<sup>84</sup> The smaller bandgap may be more conducive to the transfer of photogenerated

charge carriers, effectively enhancing its photocatalytic activity. The CBM is located at the  $K$  point, whereas the VBM is positioned at the  $\Gamma$  high-symmetry point, which makes the  $\text{GeI}_2/\text{C}_2\text{N}$  heterostructure an indirect semiconductor. Furthermore, the CBM is particularly dispersive compared to the VBM, meaning that photogenerated electrons have smaller effective masses, which may increase electron–hole pair separation during the water redox reaction and photocatalytic activity. The minimum energy in the CB and the maximum energy in the VB occur at distinct crystal momentum levels in indirect bandgap semiconductors. Because the curves are parabolic, a direct electron transfer from the VB to the CB needs a photon with a larger energy than the band gap. However, it is feasible to perform an electronic transition at lower energy, but a phonon is required. Moreover, the reduced bandgap energy will benefit more visible light absorption with significant solar energy conversion efficiency and make the transfer and separation of photogenerated charge carriers easy with the contribution of phonons, which is similar to other indirect  $\text{C}_2\text{N}$ -based heterostructures, such as  $\text{InSe}/\text{C}_2\text{N}$ <sup>85</sup> and  $\text{SiC}/\text{C}_2\text{N}$ .<sup>70</sup> The bandgap value of the  $\text{GeI}_2/\text{C}_2\text{N}$  heterostructure is greater than the minimum bandgap energy (1.23 eV) necessary for photocatalysis processes,<sup>86</sup> implying that it might be used as an efficient visible light photocatalyst for  $\text{H}_2$  generation.<sup>87</sup> The density of states in Fig. 3b shows that the VBM and CBM are dominated by the  $\text{GeI}_2$  monolayer and  $\text{C}_2\text{N}$ , respectively, resulting in a type-II band alignment. Because the photogenerated charge distribution is kept in different layers and spontaneously separated at the interface, the type-II band alignment makes the  $\text{GeI}_2/\text{C}_2\text{N}$  vdW heterostructure promising as a solar energy conversion device. Furthermore to get a fundamental understanding of the electronic properties of the  $\text{GeI}_2/\text{C}_2\text{N}$  vdW heterostructure, we

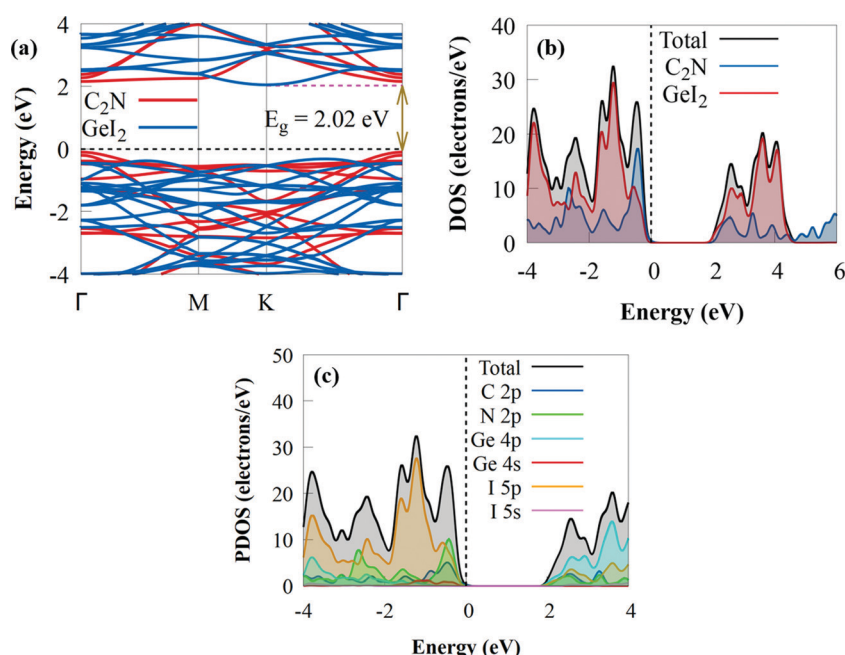


Fig. 3 (a) Projected electronic band structure, (b) DOS and (c) PDOS of the  $\text{GeI}_2/\text{C}_2\text{N}$  vdW heterostructure. The Fermi level is set to zero.



investigate the PDOS. The results demonstrate that the VBM is mostly dominated by the C 2p state, whereas the CBM is primarily from the Ge 4p state with contributions from the I 5p state, confirming the type-II band alignment (Fig. 3c). As a result, electron transfer from the C 2p orbitals of  $\text{C}_2\text{N}$  into the Ge 4p states of  $\text{GeI}_2$  monolayer is favoured.

The three-dimensional charge density difference (CDD) and the average planar potential drop ( $\Delta V$ ) in the  $z$ -direction are determined to investigate the interface impacts on the charge transfer mechanism of the  $\text{GeI}_2/\text{C}_2\text{N}$  vdW heterostructure, as given in Fig. 4a.

The CDD ( $\Delta\rho$ ) is computed by subtracting the charge densities of the  $\text{GeI}_2$  monolayer and  $\text{C}_2\text{N}$  from the charge density of the  $\text{GeI}_2/\text{C}_2\text{N}$  vdW heterostructure:

$$\Delta\rho = \rho_{\text{GeI}_2/\text{C}_2\text{N}} - \rho_{\text{GeI}_2} - \rho_{\text{C}_2\text{N}} \quad (2)$$

where the charge densities of the  $\text{GeI}_2/\text{C}_2\text{N}$  vdW heterostructure,  $\text{C}_2\text{N}$  and  $\text{GeI}_2$  monolayer are denoted by  $\rho_{\text{GeI}_2/\text{C}_2\text{N}}$ ,  $\rho_{\text{C}_2\text{N}}$  and  $\rho_{\text{GeI}_2}$ , respectively. The difference in charge density implies that the charge density is redistributed by producing hole- and electron-rich regions. Charge redistribution occurs mostly across the constituent layers of the vdW heterostructure due to the weak vdW interaction and built-in electric field. Correspondingly, the negative (green) and positive (yellow) charge values represent charge depletion and accumulation, respectively, at that position. To consider the charge distribution after the formation of the heterojunction, the planar-averaged charge density difference of the  $\text{GeI}_2/\text{C}_2\text{N}$  vdW heterostructure along the  $z$ -direction was calculated, as shown in Fig. 4b. The charge density is accumulated close to the  $\text{GeI}_2$  monolayer due

to the positive charge density and depleted near the  $\text{C}_2\text{N}$  because of the negative charge density. Therefore, the charge density difference between the  $\text{GeI}_2$  monolayer and the  $\text{C}_2\text{N}$  interface shows that the  $\text{C}_2\text{N}$  donates electrons, while the  $\text{GeI}_2$  monolayer serves as an electron acceptor. Detailed calculations of charge density across the interface revealed that 0.197 electrons transfer from the  $\text{C}_2\text{N}$  to the  $\text{GeI}_2$  monolayer based on the Löwdin population charge analysis.<sup>88</sup> The weak vdW forces and strong built-in electrostatic field in the interfacial area of the  $\text{GeI}_2/\text{C}_2\text{N}$  vdW heterostructure<sup>89</sup> are explained by such a small charge transfer. The potential drop ( $\Delta V$ ) along the  $z$ -direction of the  $\text{GeI}_2/\text{C}_2\text{N}$  vdW heterostructure is illustrated in Fig. 4c to help in comprehending the underlying cause of the charge transfer. There is a significant electrostatic potential difference between the  $\text{GeI}_2$  monolayer and  $\text{C}_2\text{N}$ , with the  $\text{C}_2\text{N}$  having a higher potential than the  $\text{GeI}_2$  monolayer. A strong built-in electric field pointing from  $\text{C}_2\text{N}$  to  $\text{GeI}_2$  is created by such a distinct electrostatic potential, which may significantly increase charge transfer and carrier dynamics, reducing the recombination rate of photoinduced charge carriers. This will help in improving photocatalytic activity. Generally, charge transfers occur from a higher potential to a lower potential based on the difference in their electrostatic potentials. Because the  $\text{C}_2\text{N}$  has a higher potential than the  $\text{GeI}_2$  monolayer, charge transfers from the  $\text{C}_2\text{N}$  to the  $\text{GeI}_2$  monolayer. This is in agreement with the CDD results. The built-in electric field creates a large  $\Delta V$  of 7.16 eV across the heterostructure interface and the light-excited electrons are easily transferred from  $\text{C}_2\text{N}$  to the  $\text{GeI}_2$  monolayer, due to the higher electrostatic potential of the  $\text{C}_2\text{N}$  layer.<sup>26,90,91</sup> Moreover, such a large  $\Delta V$  at

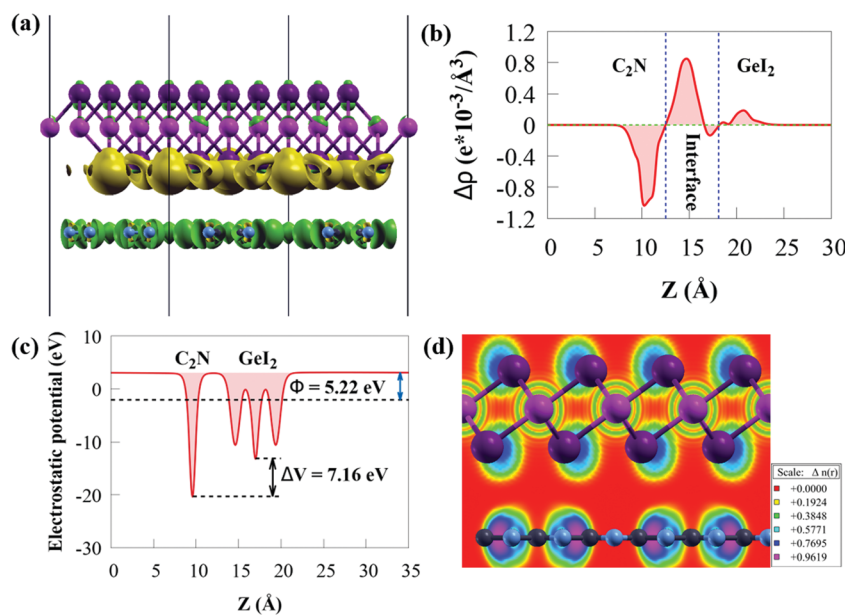


Fig. 4 (a) Three-dimensional charge density difference of the  $\text{GeI}_2/\text{C}_2\text{N}$  vdW heterostructure with an isovalue of  $0.0008 \text{ e bohr}^{-3}$ . Green and yellow isosurfaces denote charge depletion and accumulation, respectively. (b) The averaged difference in the electron density for the  $\text{GeI}_2/\text{C}_2\text{N}$  vdW heterostructure along the  $z$ -axis. The inner surfaces of the two materials are marked with a blue dashed line. (c) The potential drop ( $\Delta V$ ) for the  $\text{GeI}_2/\text{C}_2\text{N}$  vdW heterostructure. (d) Electron localisation functions across the  $\text{GeI}_2/\text{C}_2\text{N}$  vdW heterostructure interface. Grey, blue, magenta and purple balls denote C, N, Ge and I atoms, respectively.



the interface is an efficient driving force to boost photoexcited charge carrier transfer and improve the solar conversion efficiency. Moreover, the weak interfacial interaction across the  $\text{GeI}_2/\text{C}_2\text{N}$  heterostructure interface can also be visualised by analysing the corresponding electron localisation function, as shown in Fig. 4d. We observe no electrons in the interface region, confirming the weak vdW interaction in the  $\text{GeI}_2/\text{C}_2\text{N}$  heterostructure.

The work function ( $\Phi$ ) is an important parameter to comprehend charge separation and transfer at the  $\text{GeI}_2/\text{C}_2\text{N}$  vdW heterostructure interface.  $\Phi$  was calculated by aligning the Fermi energy to the vacuum energy:

$$\Phi = E_{\text{vacuum}} - E_{\text{Fermi}}, \quad (3)$$

where  $E_{\text{vacuum}}$  and  $E_{\text{Fermi}}$  represent the electrostatic potentials of the vacuum and Fermi energy levels, respectively. The calculated  $\Phi$  values are 6.21, 5.70 and 5.22 eV for the  $\text{GeI}_2$  monolayer,  $\text{C}_2\text{N}$  and the  $\text{GeI}_2/\text{C}_2\text{N}$  vdW heterostructure, respectively, as shown in Fig. 4c and 5.

When the  $\text{GeI}_2/\text{C}_2\text{N}$  vdW heterostructure is constructed by stacking the  $\text{GeI}_2$  monolayer and  $\text{C}_2\text{N}$  together perpendicular to the 2D plane, electrons will transfer from the  $\text{C}_2\text{N}$  to the  $\text{GeI}_2$  due to the higher  $\Phi$  of the  $\text{GeI}_2$  monolayer. Accordingly, the  $\text{C}_2\text{N}$  and the  $\text{GeI}_2$  monolayer are positively and negatively charged, respectively, across the interfacial region. The  $\Phi$  of the  $\text{GeI}_2/\text{C}_2\text{N}$  vdW heterostructure lies between the  $\text{C}_2\text{N}$  and the  $\text{GeI}_2$  monolayer. With an increase in electron transfer, the Fermi energies of  $\text{C}_2\text{N}$  and the  $\text{GeI}_2$  monolayer shift upwards and reach the same level after interface equilibrium. The lower  $\Phi$  in the vdW heterostructure corresponds to an efficient interfacial electron transfer, which induces a built-in electric field, reducing the recombination rate of charge carriers. Moreover, the difference in the  $\Phi$  values between the  $\text{GeI}_2$  monolayer and  $\text{C}_2\text{N}$  induces charge redistribution at the interface.

The band bending ( $\Delta E_{\text{band bending}}$ ) is evaluated to further understand the charge transfer:<sup>92</sup>

$$\Delta E_{\text{band bending}} = \Phi_{\text{HS}} - \Phi_{\text{ML}} \quad (4)$$

where  $\Phi_{\text{HS}}$  and  $\Phi_{\text{ML}}$  are the work functions of the  $\text{GeI}_2/\text{C}_2\text{N}$  vdW heterostructure and the isolated monolayers, respectively. The  $\Delta E_{\text{band bending}}$  values were calculated as -0.991 and -0.483 eV for the  $\text{GeI}_2$  monolayer and  $\text{C}_2\text{N}$ , respectively. The calculated  $\Delta E_{\text{band bending}}$  values are less than 0, suggesting electron

transfer from the heterostructure to the monolayer.<sup>93</sup> We observed that  $\Delta E_{\text{band bending}}$  of the  $\text{GeI}_2$  monolayer was more negative compared to that of the  $\text{C}_2\text{N}$ . Therefore, the net Löwdin population charge on the  $\text{GeI}_2$  monolayer is positive, consistent with the CDD and work function results.

Another critical element in constructing photocatalytic devices is optical absorption. A broad and strong absorption edge is required to achieve efficient solar energy conversion during water splitting processes. The initial stage in water splitting is photon absorption, which produces electron-hole pairs. A strong visible light-harvesting capacity and appropriate electronic and interface properties are required for promising photocatalytic materials. With this in mind, the optical properties of the  $\text{GeI}_2/\text{C}_2\text{N}$  vdW heterostructure are calculated to access its photocatalytic application. It is clear that the  $\text{GeI}_2$  monolayer slightly absorbs visible light. But the visible light absorption coefficient of  $\text{C}_2\text{N}$  is higher than that of the  $\text{GeI}_2$  monolayer (Fig. 6).

Considering the influence of interface contact on the optical properties, we compared the absorption coefficients of the  $\text{GeI}_2/\text{C}_2\text{N}$  vdW heterostructure to those of the  $\text{C}_2\text{N}$  and the  $\text{GeI}_2$  monolayer. As expected, the vdW heterostructure shows a higher redshift around 720 nm than the individual monolayers, which is particularly useful for capturing solar energy. This enhancement is due to its narrower bandgap energy than the  $\text{GeI}_2$  monolayer and  $\text{C}_2\text{N}$ . The efficient absorption of solar light for the  $\text{GeI}_2/\text{C}_2\text{N}$  vdW heterostructure mainly results from the coupling activity between the  $\text{GeI}_2$  and  $\text{C}_2\text{N}$ , including the electron transfer from  $\text{C}_2\text{N}$  to the  $\text{GeI}_2$  monolayer and the charge redistribution at the interface.<sup>79</sup> Therefore, the  $\text{GeI}_2/\text{C}_2\text{N}$  vdW heterostructure is more effective in utilising solar energy, which holds great promise in visible light-harvesting photocatalytic devices.

Furthermore, the proper band position for water redox potentials is a key criterion for photocatalytic water splitting, where the VBM and CBM must be lower and higher than the  $\text{O}_2$  (-5.67 eV) and  $\text{H}_2$  (-4.44 eV) potentials at pH = 0, respectively.<sup>94</sup> The CBMs for the  $\text{GeI}_2$  monolayer,  $\text{C}_2\text{N}$  and the  $\text{GeI}_2/\text{C}_2\text{N}$  vdW heterostructure are -4.33, -4.07 and -4.02 eV, respectively, while their VBMs are -7.36, -6.31 and -5.98 eV, respectively. This demonstrates that all of these materials meet the overall water splitting criteria. The high bandgap of the  $\text{GeI}_2$  monolayer, on the other hand, substantially restricts its

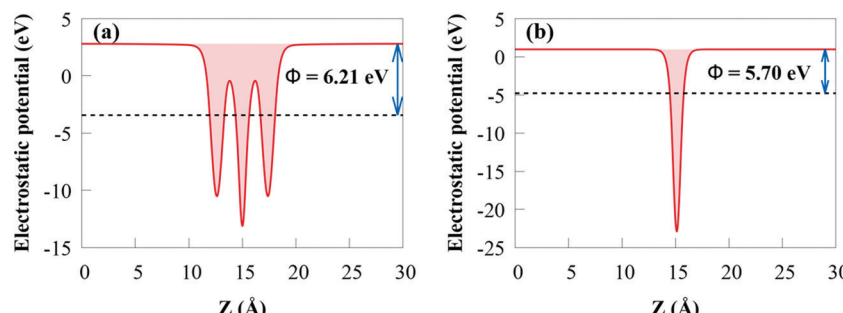


Fig. 5 Work function for (a) the  $\text{GeI}_2$  monolayer and (b)  $\text{C}_2\text{N}$ .



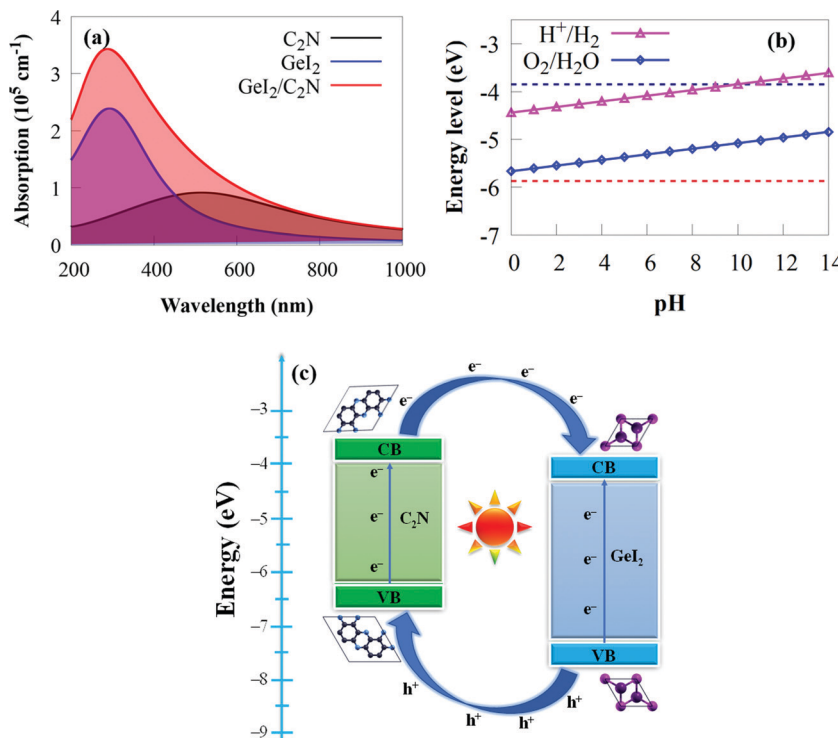


Fig. 6 (a) Calculated absorption spectra of the  $2 \times 2$  supercell of  $\text{C}_2\text{N}$ , the  $4 \times 4$  supercell of  $\text{GeI}_2$  and the  $\text{GeI}_2/\text{C}_2\text{N}$  vdW heterostructure. (b) The absolute energy bands for the conduction band minimum and valence band minimum of the  $\text{GeI}_2/\text{C}_2\text{N}$  vdW heterostructure with respect to pH (0–14). (c) Schematic diagram showing the transfer of photogenerated electrons and holes.

efficiency in solar energy utilisation. Because  $\text{C}_2\text{N}$  lacks an electric field, it has a fast electron–hole pair recombination rate,<sup>25,26,37</sup> which is unfavourable for photocatalysis. The CBM and VBM potentials of the  $\text{GeI}_2/\text{C}_2\text{N}$  vdW heterostructure are 0.442 eV and 0.308 eV higher and lower than the  $\text{H}^+/\text{H}_2$  reduction and  $\text{O}_2/\text{H}_2\text{O}$  oxidation potentials at pH = 0, respectively, which is sufficient for  $\text{H}_2$  and  $\text{O}_2$  generation. As a result, the  $\text{GeI}_2/\text{C}_2\text{N}$  vdW heterostructure straddles the water redox potentials at pH = 0. Furthermore, pH has an effect on the redox potential of water.<sup>95</sup> The  $\text{H}^+/\text{H}_2$  and  $\text{O}_2/\text{H}_2\text{O}$  potentials are calculated as  $-4.44 \text{ eV} + \text{pH} \times 0.059 \text{ eV}$  and  $-5.67 + \text{pH} \times 0.059 \text{ eV}$ , respectively.<sup>95</sup> Furthermore, the band edges of the  $\text{GeI}_2/\text{C}_2\text{N}$  vdW heterostructure in comparison to aqueous solution straddle the water redox potential at pH values ranging from 0 to 9 (Fig. 6b). This suggests that the  $\text{GeI}_2/\text{C}_2\text{N}$  vdW heterostructure may be a better water splitting material, whether under acidic, neutral or alkaline environments without an external bias voltage.

The spatial separation of charge carriers at the  $\text{GeI}_2/\text{C}_2\text{N}$  vdW heterostructure interface is investigated further. The VBM (CBM) of  $\text{C}_2\text{N}$  is lower (higher) than that of the  $\text{GeI}_2$  monolayer, as shown in the schematic diagram in Fig. 6c, allowing us to establish a type-II band alignment of the vdW heterostructure. In solar conversion and optoelectronic devices, the conduction band offset (CBO) and valence band offset (VBO) are critical. The VBO and CBO of the  $\text{GeI}_2/\text{C}_2\text{N}$  vdW heterostructure are calculated as 1.05 and 0.26 eV, respectively. Under light irradiation, the photogenerated particles get energy from photons to

excite the photogenerated electrons in the VBs of both monolayers and transfer them to their CBs by creating holes in the VBs. The band offset will allow the transport of photoinduced holes from the VB of the  $\text{GeI}_2$  monolayer to the VB of  $\text{C}_2\text{N}$  and photoinduced electrons from the CB of  $\text{C}_2\text{N}$  to the CB of the  $\text{GeI}_2$  monolayer, thereby reducing photogenerated charge carrier recombination. As a result, both the VBO and CBO can improve photogenerated charge carrier separation.<sup>96</sup> Because the CBM is located on the  $\text{GeI}_2$  monolayer, the OER will mostly take place on it, whereas the HER will take place on the  $\text{C}_2\text{N}$ .

Applying external strain has been an efficient technique to tune the electronic, optical and structural properties of 2D vdW heterostructures,<sup>97</sup> which is beneficial in photocatalysis, optoelectronic and nanoelectronic devices.<sup>98</sup> Herein, we investigate the effect of biaxial strain on the electronic, optical and structural properties of the  $\text{GeI}_2/\text{C}_2\text{N}$  vdW heterostructure by varying the lattice parameters as follows:

$$\varepsilon = [(a_0 - a_1)/a_1] \times 100\%,$$

where  $a_1$  and  $a_0$  are the lattice constants of the  $\text{GeI}_2/\text{C}_2\text{N}$  vdW heterostructure before and after the applied strain, respectively. An in-plane biaxial strain from  $-8\%$  to  $+8\%$  is applied in this study. Before studying the effect of the biaxial strain on the electronic properties, the strain energy ( $E_s$ ) is initially examined as follows:

$$E_s = E_{\text{strain}} - E_{\text{unstrain}} \quad (5)$$



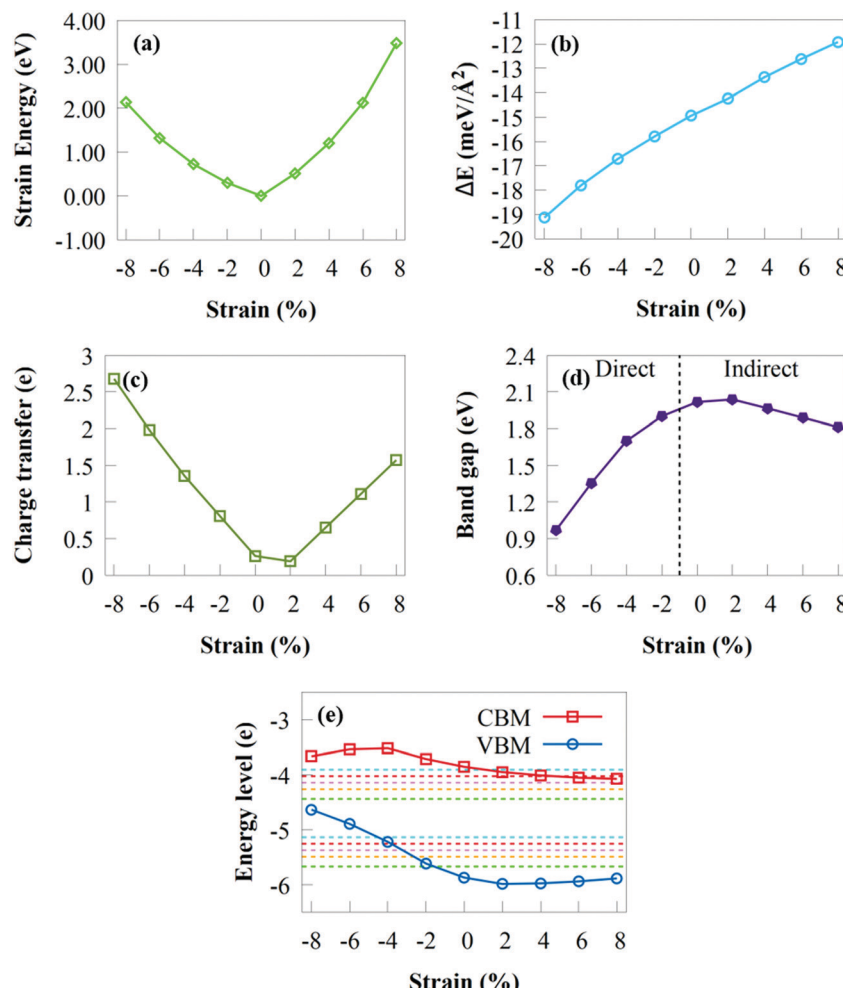


Fig. 7 (a) Strain energy, (b) binding energy, (c) charge transfer, (d) bandgap energies and (e) band edges of the  $\text{GeI}_2/\text{C}_2\text{N}$  vdW heterostructure under different biaxial strains. Green, orange, magenta, red and cyan dashed lines denote  $\text{pH} = 0, 3, 5, 7$  and  $9$ , respectively.

where  $E_{\text{strain}}$  and  $E_{\text{unstrain}}$  are the total energies for the biaxial strain and unstrained systems, respectively. When compressive or tensile biaxial strain is applied,  $E_s$  increases with increasing strain (see Fig. 7a).

As the compressive or tensile strain increases,  $E_s$  fluctuates smoothly as a quadratic curve, demonstrating that the  $\text{GeI}_2/\text{C}_2\text{N}$  vdW heterostructure has no phase transition and retains its hexagonal structure under a biaxial strain of  $\pm 8\%$ . As a result, the imposed biaxial strain is ensured to be under the elastic limit and totally reversible.<sup>98</sup> The interface binding energy under compressive/tensile strain is given in Fig. 7b to provide a fundamental understanding of the effect of biaxial strain on the interfacial interactions. The interface binding energy remains negative under a biaxial strain of  $\pm 8\%$ , demonstrating the energy stability of the  $\text{GeI}_2/\text{C}_2\text{N}$  heterostructure. The stability increases when the compressive strain varies from  $-2\%$  to  $-8\%$ , whereas it decreases when the tensile strain changes from  $+2\%$  to  $+8\%$ . This suggests that the  $\text{GeI}_2/\text{C}_2\text{N}$  vdW heterostructure is more stable with an increasing/decreasing compressive/tensile biaxial strain.

The amount of charge transfer at the  $\text{GeI}_2/\text{C}_2\text{N}$  vdW heterostructure interface under biaxial strain is shown in Fig. 7c. The

positive  $\Delta Q$  values indicate that electrons are transferred from the  $\text{C}_2\text{N}$  to the  $\text{GeI}_2$  monolayer under compressive/tensile biaxial strain. Therefore, a built-in electric field may occur in a biaxial strain of  $\pm 8\%$ .  $\Delta Q$  of the  $\text{GeI}_2/\text{C}_2\text{N}$  vdW heterostructure decreases with a tensile strain of  $+2\%$ , while it increases when the tensile strain increases from  $+4\%$  to  $+8\%$ . This is in agreement with the bandgap energy obtained shown in Fig. 7d. Moreover, it increases from  $0.809e$  to  $2.697e$  with a compressive strain from  $-2\%$  to  $-8\%$ .

Fig. 7d depicts the fluctuation of the bandgap energies in the  $\text{GeI}_2/\text{C}_2\text{N}$  vdW heterostructure under biaxial strains from  $+8\%$  to  $-8\%$ . When the tensile biaxial strain is less than  $+2\%$ , the bandgap energy of the  $\text{GeI}_2/\text{C}_2\text{N}$  vdW heterostructure slightly increases. Obviously, tensile biaxial strains from  $+4\%$  to  $+8\%$  monotonically decrease the bandgap energy due to the increasing amount of charge transferring at the heterostructure interface, while the indirect bandgap energy remains unchanged. Electrons in semiconductors with a reduced bandgap are less likely to recombine during charge transfer, which is critical in solar conversion devices. Compared with the unstrained system, tensile biaxial strains from  $+4\%$  to  $+8\%$



reduce the  $\text{GeI}_2/\text{C}_2\text{N}$  vdW heterostructure bandgap, which indicates the importance of biaxial strain in tuning the bandgap of the  $\text{GeI}_2/\text{C}_2\text{N}$  vdW heterostructure. The smaller bandgap observed under tensile biaxial strain is more conducive to solar energy conversion because the energy required to excite electrons from the VB to the CB of the heterostructure is smaller. The bandgap energy decreases linearly with a compressive biaxial strain. This shows the different variation patterns of the bandgap energy under compressive strain.

Fig. 7e depicts the fluctuation of the band edges of the  $\text{GeI}_2/\text{C}_2\text{N}$  vdW heterostructure under various biaxial strains and pH. The heterostructure has an appropriate band edge position for overall water splitting at pH 0 to 5 under an applied biaxial strain range from +2% to +8%. Moreover, overall water splitting is achieved under pH 0 up to 6 and 7, respectively, under tensile strain from +2% to +4% and +2%. Clearly, as tensile strain increases, the VBM and CBM increasingly move towards the water oxidation and reduction potentials. This indicates that the reducing potential of the  $\text{GeI}_2/\text{C}_2\text{N}$  vdW heterostructure becomes weak with increasing pH, which is not favourable to generate  $\text{H}_2$  at a higher pH. Nevertheless, when compressive strain increases, the VBM steadily decreases, indicating that the oxidising power weakens. The  $\text{GeI}_2/\text{C}_2\text{N}$  heterostructure bandgap is 0.97 eV under a compressive strain of -2%, which is less than the minimum bandgap energy (1.23 eV) needed for water splitting. Nevertheless, under compressive strains from -4% to -8%, the  $\text{GeI}_2/\text{C}_2\text{N}$  vdW heterostructure is only suited for  $\text{H}_2$  generation and not for  $\text{O}_2$  generation. The VBM is lower than the  $\text{H}_2\text{O}/\text{O}_2$  potential at pH 3 to 7, indicating that the system may achieve overall water splitting under a compressive strain of -2%. The favourable band edge position suggests that the  $\text{GeI}_2/\text{C}_2\text{N}$  vdW heterostructure has strong tensile strain resistance for overall water splitting.

We computed the phonon spectra under biaxial strain ranging from -8% to +8% to ensure that the  $\text{GeI}_2/\text{C}_2\text{N}$  vdW heterostructure is dynamically stable throughout the tensile strain range. As seen in Fig. S1 (ESI†), phonon dispersion spectra reveal positive frequencies, suggesting the dynamic stability of the  $\text{GeI}_2/\text{C}_2\text{N}$  vdW heterostructure under biaxial strain.

The band structure of the  $\text{GeI}_2/\text{C}_2\text{N}$  vdW heterostructure under biaxial strain from +8% to -8% is shown in Fig. S2 (ESI†). The CBM and VBM are fixed at the  $\Gamma$  high-symmetry point when the tensile biaxial strain changes from +2% to +8%, indicating that the type-II indirect bandgap nature of the unstrained  $\text{GeI}_2/\text{C}_2\text{N}$  vdW heterostructure has altered dramatically. Thus, tensile biaxial strain pushed the sub-bands in the CB of  $\text{C}_2\text{N}$  closer to the Fermi energy. As tensile strain increases from +2% to +8%, the position of the CBM progressively shifted from the  $K$  to  $\Gamma$  point, resulting in the type-II indirect to type-I direct band structure transition. Because the CBM and VBM of semiconductor 1 lie between the CBM and VBM of semiconductor 2 in the type-I vdW heterostructure, charge carriers are spatially localised in the same component, which efficiently promotes charge carrier recombination and lowers their separation. Thus, the type-I vdW heterostructure is more

suitable for light-emitting diodes and lasers.<sup>99</sup> The type-II indirect band structure of the  $\text{GeI}_2/\text{C}_2\text{N}$  vdW heterostructure, however, remains intact during compressive strain engineering, as seen in Fig. S2 (ESI†). This increases the charge carrier lifetime, which could be useful in optoelectronic, photoelectric, and solar energy conversion devices.<sup>100</sup> Thus, the band alignment transition makes the  $\text{GeI}_2/\text{C}_2\text{N}$  vdW heterostructure promising for application in multi-functional devices. Also, flat bands can occur along the  $\Gamma\text{--}M\text{--}K\text{--}\Gamma$  Brillouin zone under a larger compressive strain from -4% to -8%. This illustrates that a large compressive biaxial strain of -8% may push the valence band extrema (VBE) along the  $\Gamma\text{--}K$  or  $\Gamma\text{--}M$  direction near the VBM. The formation of flat bands around the VBM has been reported in other strained 2D materials.<sup>101,102</sup>

Under tensile strain, the C 2p and N 2p orbitals contribute significantly to the CBM and VBM as illustrated in Fig. S3 (ESI†). This shows that the type-II band alignment changes dramatically under tensile biaxial strain. On the other hand, a compressive biaxial strain of -2% to -8% did not affect the orbital contributions at the VBM and CBM. The N 2p and Ge 4p orbitals contributed to the VBM and CBM, respectively. Considering the electronic transition selection rules, the electrons are primarily excited from the N 2p orbitals to the Ge 4p orbitals, making the system type-II. We observed that the electronic properties of the  $\text{GeI}_2/\text{C}_2\text{N}$  vdW heterostructure respond sensitively to compressive biaxial strain by investigating the PDOS and band structure, causing the  $\text{GeI}_2/\text{C}_2\text{N}$  vdW heterostructure to transition from a type-II indirect to type-I direct electronic band structure.

Fig. S4 (ESI†) depicts the computed DOS of the  $\text{GeI}_2/\text{C}_2\text{N}$  vdW heterostructure with biaxial strain. When tensile biaxial strain changes from +2% to +8%, we see that  $\text{C}_2\text{N}$  contributes the most to the VBM and CBM, confirming that the system is a type-I heterostructure. Fig. S4 (ESI†) shows that the type-II heterojunction is retained when the compressive strain varies from -2% to -8%.

## IV. Conclusions

To explore the potential applications in photocatalysis, we explored the work function, band structure, optical properties, band alignment, charge transfer and band offset of the proposed 2D vertical  $\text{GeI}_2/\text{C}_2\text{N}$  vdW heterostructure using DFT calculations. By assessing its interface binding energy, AIMD simulation and vibrational phonon spectra at room temperature, the vdW heterostructure was created by weak vdW forces with thermal and dynamic stability. Furthermore, the small lattice mismatch confirms the experimental realisation of the  $\text{GeI}_2/\text{C}_2\text{N}$  vdW heterostructure. The proposed heterostructure is found to have a conventional type-II band alignment with an indirect bandgap of 2.02 eV and electrons tend to move from the  $\text{C}_2\text{N}$  to the  $\text{GeI}_2$  monolayer. Besides, the charge density difference analysis showed that  $\text{C}_2\text{N}$  transferred about  $0.263|e|$  to the  $\text{GeI}_2$  monolayer. Furthermore, the  $\text{GeI}_2/\text{C}_2\text{N}$  vdW heterostructure exhibits high visible light absorption



due to its smaller bandgap as compared to those of the isolated  $\text{GeI}_2$  monolayer and  $\text{C}_2\text{N}$ . The band edges of the  $\text{GeI}_2/\text{C}_2\text{N}$  vdW heterostructure met the criteria of overall water splitting at a pH range of 0 to 9. Furthermore, the potential drop of 7.16 eV and the built-in electric field at the interface help in the effective separation of photoinduced electron-hole pairs. Under tensile biaxial strain, the band alignment changes from a type-II indirect to type-I direct band alignment. Our theoretical findings offer fundamental insights into designing solar conversion and other high performance optoelectronic or electronic devices.

## Conflicts of interest

The authors declare no conflicts of interest.

## Acknowledgements

This research was performed using the computational facilities provided by the Centre for High Performance Computing (CHPC), Cape Town, South Africa.

## References

- 1 A. S. Arico, P. Bruce, B. Scrosati, J.-M. Tarascon and W. Van Schalkwijk, *Mater. Sustainable Energy Appl.*, 2011, **148**–159.
- 2 G. Kumar, S.-H. Kim, C.-H. Lay and V. K. Ponnusamy, *Bioresour. Technol.*, 2020, **317**, 124010.
- 3 I. Shahid, S. Ahmad, N. Shehzad, S. Yao, C. V. Nguyen, L. Zhang and Z. Zhou, *Appl. Surf. Sci.*, 2020, **523**, 146483.
- 4 N. Shehzad, I. Shahid, S. Yao, S. Ahmad, A. Ali, L. Zhang and Z. Zhou, *Int. J. Hydrogen Energy*, 2020, **45**, 27089–27097.
- 5 I. Shahid, A. Ali, J.-M. Zhang, I. Muhammad, I. Ahmad and F. Kabir, *Int. J. Hydrogen Energy*, 2021, **46**, 14247–14258.
- 6 R. Varunaa and P. Ravindran, *Phys. Chem. Chem. Phys.*, 2019, **21**, 25311–25322.
- 7 A. Fujishima and K. Honda, *Nature*, 1972, **238**, 37–38.
- 8 A. R. Amani-Ghadim, F. Khodam and M. S. S. Dorraji, *J. Mater. Chem. A*, 2019, **7**, 11408–11422.
- 9 Z. Cui, N. Lyu, Y. Ding and K. Bai, *Phys. E*, 2021, **127**, 114503.
- 10 J. Li, Z. Huang, W. Ke, J. Yu, K. Ren and Z. Dong, *J. Alloys Compd.*, 2021, **866**, 158774.
- 11 Z. Ma, B. Wang, L. Ou, Y. Zhang, X. Zhang and Z. Zhou, *Nanotechnology*, 2016, **27**, 415203.
- 12 F. Opoku, K. K. Govender, C. G. C. E. van Sittert and P. P. Govender, *New J. Chem.*, 2017, **41**, 8140–8155.
- 13 D. K. Pham, S.-T. Nguyen and C. Q. Nguyen, *New J. Chem.*, 2021, **45**, 15942–15948.
- 14 K. Zheng, H. Cui, H. Luo, J. Yu, S. Wang, C. Tan, L. Wang, X. Li, L.-Q. Tao and X. Chen, *J. Mater. Chem. C*, 2020, **8**, 11980–11987.
- 15 H. L. Zhuang, M. D. Johannes, M. N. Blonsky and R. G. Hennig, *Appl. Phys. Lett.*, 2014, **104**, 022116.
- 16 J. Mahmood, E. K. Lee, M. Jung, D. Shin, I.-Y. Jeon, S.-M. Jung, H.-J. Choi, J.-M. Seo, S.-Y. Bae and S.-D. Sohn, *Nat. Commun.*, 2015, **6**, 1–7.
- 17 P. Netrattana and P. Reunchan, *J. Phys.: Conf. Ser.*, 2017, **901**, 012102.
- 18 L. Wang, W. Si, Y. Tong, F. Hou, D. Pergolesi, J. Hou, T. Lippert, S. X. Dou and J. Liang, *Carbon Energy*, 2020, **2**, 223–250.
- 19 B. Peng, L. Xu, J. Zeng, X. Qi, Y. Yang, Z. Ma, X. Huang, L.-L. Wang and C. Shuai, *Catal. Sci. Technol.*, 2021, **11**, 3059–3069.
- 20 W. Wei and T. Jacob, *Phys. Rev. B: Condens. Matter Mater. Phys.*, 2013, **87**, 085202.
- 21 J. Mahmood, F. Li, S.-M. Jung, M. S. Okyay, I. Ahmad, S.-J. Kim, N. Park, H. Y. Jeong and J.-B. Baek, *Nat. Nanotechnol.*, 2017, **12**, 441–446.
- 22 R. Wu, K. Zhou, C. Y. Yue, J. Wei and Y. Pan, *Prog. Mater. Sci.*, 2015, **72**, 1–60.
- 23 H. Ozisik, K. Colakoglu, H. B. Ozisik and E. Deligoz, *Comput. Mater. Sci.*, 2010, **50**, 349–355.
- 24 L. Xu, Z. Ma, Q. Li, T. Chen, B. Peng, J. Zeng, Y. Zhang, K.-W. Luo, L.-L. Wang and C. Shuai, *New J. Chem.*, 2020, **44**, 15439–15445.
- 25 C. Li, Y. Xu, W. Sheng, W.-J. Yin, G.-Z. Nie and Z. Ao, *Phys. Chem. Chem. Phys.*, 2020, **22**, 615–623.
- 26 G. Wang, Z. Li, W. Wu, H. Guo, C. Chen, H. Yuan and S. A. Yang, *Phys. Chem. Chem. Phys.*, 2020, **22**, 24446–24454.
- 27 S. J. Liang, B. Cheng, X. Cui and F. Miao, *Adv. Mater.*, 2020, **32**, 1903800.
- 28 Y. Gan, J. Liang, C.-W. Cho, S. Li, Y. Guo, X. Ma, X. Wu, J. Wen, X. Du and M. He, *Front. Phys.*, 2020, **15**, 1–7.
- 29 G. X. Zheng, J. M. Terry, P. Belgrader, P. Ryvkin, Z. W. Bent, R. Wilson, S. B. Ziraldo, T. D. Wheeler, G. P. McDermott and J. Zhu, *Nat. Commun.*, 2017, **8**, 1–12.
- 30 M. U. Farooq, V. Novosad, E. A. Rozhkova, H. Wali, A. Ali, A. A. Fateh, P. B. Neogi, A. Neogi and Z. Wang, *Sci. Rep.*, 2018, **8**, 1–12.
- 31 Z. Zhang, Y. Zhang, Z. Xie, X. Wei, T. Guo, J. Fan, L. Ni, Y. Tian, J. Liu and L. Duan, *Phys. Chem. Chem. Phys.*, 2019, **21**, 5627–5633.
- 32 F. Opoku, O. Akoto, S. O.-B. Oppong and A. A. Adimado, *New J. Chem.*, 2021, **45**, 20365–20373.
- 33 H. Zhou, W. Cai, J. Li, X. Liu, W. Xiong, Y. Zhou, Z. Xu, B. Wang and C. Ye, *Phys. Chem. Chem. Phys.*, 2020, **22**, 1485–1492.
- 34 R. Zhang, L. Zhang, Q. Zheng, P. Gao, J. Zhao and J. Yang, *J. Phys. Chem. Lett.*, 2018, **9**, 5419–5424.
- 35 Z. Zheng, X. Wang and W. Mi, *Carbon*, 2017, **117**, 393–398.
- 36 X. Zhang, A. Chen, Z. Zhang, M. Jiao and Z. Zhou, *Nanoscale Adv.*, 2019, **1**, 154–161.
- 37 Y. Bai, Q. Zhang, N. Xu, K. Deng and E. Kan, *J. Phys. Chem. C*, 2018, **122**, 15892–15902.
- 38 H. Wang, X. Li and J. Yang, *ChemPhysChem*, 2016, **17**, 2100–2104.
- 39 R. Kumar, D. Das and A. K. Singh, *J. Catal.*, 2018, **359**, 143–150.



40 Z. Guan, C.-S. Lian, S. Hu, S. Ni, J. Li and W. Duan, *J. Phys. Chem. C*, 2017, **121**, 3654–3660.

41 S. E. Tsoeu, F. Opoku and P. P. Govender, *J. Electron. Mater.*, 2021, **50**, 620–628.

42 S. E. Tsoeu, F. Opoku and P. P. Govender, *SN Appl. Sci.*, 2020, **2**, 341.

43 G. Onida, L. Reining and A. Rubio, *Rev. Mod. Phys.*, 2002, **74**, 601.

44 V. Turkowski, N. U. Din and T. S. Rahman, *Computation*, 2017, **5**, 39.

45 E. Runge and E. K. Gross, *Phys. Rev. Lett.*, 1984, **52**, 997.

46 W. Hanke and L. J. Sham, *Phys. Rev. B: Condens. Matter Mater. Phys.*, 1980, **21**, 4656–4673.

47 Z. Wang, Y. Zhang, X. Wei, T. Guo, J. Fan, L. Ni, Y. Weng, Z. Zha, J. Liu and Y. Tian, *Phys. Chem. Chem. Phys.*, 2020, **22**, 9647–9655.

48 H. M. Tang, A.-A. Sun and S.-P. Gao, *Phys. Rev. Mater.*, 2020, **4**, 084004.

49 F. Opoku and P. P. Govender, *Mater. Chem. Phys.*, 2019, **224**, 107–116.

50 D. M. Hoat, T. V. Vu, M. M. Obeid and H. R. Jappor, *Chem. Phys.*, 2019, **527**, 110499.

51 P. Giannozzi, O. Andreussi, T. Brumme, O. Bunau, M. Buongiorno Nardelli, M. Calandra, R. Car, C. Cavazzoni, D. Ceresoli, M. Cococcioni, N. Colonna, I. Carnimeo, A. Dal Corso, S. de Gironcoli, P. Delugas, R. A. DiStasio, A. Ferretti, A. Floris, G. Fratesi, G. Fugallo, R. Gebauer, U. Gerstmann, F. Giustino, T. Gorni, J. Jia, M. Kawamura, H. Y. Ko, A. Kokalj, E. Küçükbenli, M. Lazzeri, M. Marsili, N. Marzari, F. Mauri, N. L. Nguyen, H. V. Nguyen, A. Otero-de-la-Roza, L. Paulatto, S. Poncé, D. Rocca, R. Sabatini, B. Santra, M. Schlipf, A. P. Seitsonen, A. Smogunov, I. Timrov, T. Thonhauser, P. Umari, N. Vast, X. Wu and S. Baroni, *J. Phys.: Condens. Matter*, 2017, **29**, 465901.

52 J. P. Perdew, K. Burke and M. Ernzerhof, *Phys. Rev. Lett.*, 1996, **77**, 3865–3868.

53 W. H. Press, B. P. Flannery, S. A. Teukolsky, W. T. Vetterling and P. B. Kramer, *Numerical recipes*, Cambridge University Press, Cambridge, 1989.

54 D. Hamann, *Phys. Rev. B: Condens. Matter Mater. Phys.*, 2013, **88**, 085117.

55 S. Grimme, J. Antony, S. Ehrlich and H. Krieg, *J. Chem. Phys.*, 2010, **132**, 154104.

56 S. Grimme, S. Ehrlich and L. Goerigk, *J. Comput. Chem.*, 2011, **32**, 1456–1465.

57 H. J. Monkhorst and J. D. Pack, *Phys. Rev. B: Condens. Matter Mater. Phys.*, 1976, **13**, 5188–5192.

58 S. Baroni, S. de Gironcoli, A. Dal Corso and P. Giannozzi, *Rev. Mod. Phys.*, 2001, **73**, 515–562.

59 S. Kümmel and L. Kronik, *Rev. Mod. Phys.*, 2008, **80**, 3–60.

60 J. Heyd, G. E. Scuseria and M. Ernzerhof, *J. Chem. Phys.*, 2003, **118**, 8207–8215.

61 A. A. Mostofi, J. R. Yates, G. Pizzi, Y.-S. Lee, I. Souza, D. Vanderbilt and N. Marzari, *Comput. Phys. Commun.*, 2014, **185**, 2309–2310.

62 X. Ge, S. J. Binnie, D. Rocca, R. Gebauer and S. Baroni, *Comput. Phys. Commun.*, 2014, **185**, 2080–2089.

63 O. B. Malcioglu, R. Gebauer, D. Rocca and S. Baroni, *Comput. Phys. Commun.*, 2011, **182**, 1744–1754.

64 S. Nosé, *J. Chem. Phys.*, 1984, **81**, 511–519.

65 W. G. Hoover, *PhRvA*, 1985, **31**, 1695–1697.

66 A. Kokalj, *J. Mol. Graphics Modell.*, 1999, **17**, 176–179.

67 G. Wang, Z. Li, W. Wu, H. Guo, C. Chen, H. Yuan and S. A. Yang, *Phys. Chem. Chem. Phys.*, 2020, **22**, 24446–24454.

68 H. M. Powell and F. M. Brewer, *J. Chem. Soc.*, 1938, 197–198.

69 D. Nafday, H. Fang, P. Jena and T. Saha-Dasgupta, *Phys. Chem. Chem. Phys.*, 2019, **21**, 21128–21135.

70 L. Xu, Z. Ma, Q. Li, T. Chen, B. Peng, J. Zeng, Y. Zhang, K.-W. Luo, L.-L. Wang and C. Shuai, *New J. Chem.*, 2020, **44**, 15439–15445.

71 J. Mahmood, E. K. Lee, M. Jung, D. Shin, I.-Y. Jeon, S.-M. Jung, H.-J. Choi, J.-M. Seo, S.-Y. Bae, S.-D. Sohn, N. Park, J. H. Oh, H.-J. Shin and J.-B. Baek, *Nat. Commun.*, 2015, **6**, 6486.

72 C.-S. Liu, X.-L. Yang, J. Liu and X.-J. Ye, *J. Phys. Chem. C*, 2018, **122**, 22137–22142.

73 J. Hu, W. Duan, H. He, H. Lv, C. Huang and X. Ma, *J. Mater. Chem. C*, 2019, **7**, 7798–7805.

74 Z. Zhang, Z. Xie, J. Liu, Y. Tian, Y. Zhang, X. Wei, T. Guo, L. Ni, J. Fan and Y. Weng, *Phys. Chem. Chem. Phys.*, 2020, **22**, 5873–5881.

75 Y. Chen and J. Washburn, *Phys. Rev. Lett.*, 1996, **77**, 4046–4049.

76 X. Zhang, A. Chen, Z. Zhang, M. Jiao and Z. Zhou, *Nanoscale Adv.*, 2019, **1**, 154–161.

77 X. Luo, G. Wang, Y. Huang, B. Wang, H. Yuan and H. Chen, *Phys. Chem. Chem. Phys.*, 2017, **19**, 28216–28224.

78 M. Ashwin Kishore, K. Larsson and P. Ravindran, *ACS Omega*, 2020, **5**, 23762–23768.

79 X.-H. Li, B.-J. Wang, H. Li, X.-F. Yang, R.-Q. Zhao, X.-T. Jia and S.-H. Ke, *New J. Chem.*, 2020, **44**, 16092–16100.

80 T. Björkman, A. Gulans, A. V. Krasheninnikov and R. M. Nieminen, *Phys. Rev. Lett.*, 2012, **108**, 235502.

81 X. Gao, Y. Shen, Y. Ma, S. Wu and Z. Zhou, *Appl. Phys. Lett.*, 2019, **114**, 093902.

82 Z. Zhu, K. Ren, H. Shu, Z. Cui, Z. Huang, J. Yu and Y. Xu, *Catalysts*, 2021, **11**, 991.

83 M. Idrees, C. V. Nguyen, H. Bui, I. Ahmad and B. Amin, *Phys. Chem. Chem. Phys.*, 2020, **22**, 20704–20711.

84 J. Song, H. Zheng, M. Liu, G. Zhang, D. Ling and D. Wei, *Phys. Chem. Chem. Phys.*, 2021, **23**, 3963–3973.

85 B. Wang, H. Yuan, J. Chang, X. Chen and H. Chen, *Appl. Surf. Sci.*, 2019, **485**, 375–380.

86 A. K. Singh, K. Mathew, H. L. Zhuang and R. G. Hennig, *J. Phys. Chem. Lett.*, 2015, **6**, 1087–1098.

87 Y. Li, Y.-L. Li, B. Sa and R. Ahuja, *Catal. Sci. Technol.*, 2017, **7**, 545–559.

88 D. Sanchez-Portal, E. Artacho and J. M. Soler, *Solid State Commun.*, 1995, **95**, 685–690.

89 C. Lei, Y. Ma, X. Xu, T. Zhang, B. Huang and Y. Dai, *J. Phys. Chem. C*, 2019, **123**, 23089–23095.



90 J. Zeng, L. Xu, Y. Yang, X. Luo, H.-J. Li, S. Xiong and L.-L. Wang, *Phys. Chem. Chem. Phys.*, 2021, **23**, 8318–8325.

91 K. Rahimi and A. Z. Moshfegh, *Phys. Chem. Chem. Phys.*, 2021, **23**, 20675–20685.

92 J. E. Padilha, A. Fazzio and A. J. R. da Silva, *Phys. Rev. Lett.*, 2015, **114**, 066803.

93 A. Singh, M. Jain and S. Bhattacharya, *Nanoscale Adv.*, 2021, **3**, 2837–2845.

94 V. Chakrapani, J. C. Angus, A. B. Anderson, S. D. Wolter, B. R. Stoner and G. U. Sumanasekera, *Sci.*, 2007, **318**, 1424–1430.

95 X. Zhang, Z. Zhang, D. Wu, X. Zhang, X. Zhao and Z. Zhou, *Small Methods*, 2018, **2**, 1700359.

96 N. Goel, R. Kumar and M. Kumar, *Nanotechnology*, 2021, **32**, 375711.

97 H. Li, H. Liu, L. Zhou, X. Wu, Y. Pan, W. Ji, B. Zheng, Q. Zhang, X. Zhuang, X. Zhu, X. Wang, X. Duan and A. Pan, *ACS Nano*, 2018, **12**, 4853–4860.

98 X.-H. Li, B.-J. Wang, X.-L. Cai, L.-W. Zhang, G.-D. Wang and S.-H. Ke, *RSC Adv.*, 2017, **7**, 28393–28398.

99 S. Nakamura, M. Senoh, N. Iwasa and S.-I. Nagahama, *JaJAP*, 1995, **34**, L797–L799.

100 K. Cheng, Y. Guo, N. Han, X. Jiang, J. Zhang, R. Ahuja, Y. Su and J. Zhao, *Appl. Phys. Lett.*, 2018, **112**, 143902.

101 H. T. T. Nguyen, V. V. Tuan, C. V. Nguyen, H. V. Phuc, H. D. Tong, S.-T. Nguyen and N. N. Hieu, *Phys. Chem. Chem. Phys.*, 2020, **22**, 11637–11643.

102 S.-D. Guo, X.-S. Guo and Y. Deng, *J. Appl. Phys.*, 2019, **126**, 154301.

